

Post-treatment selection for tailored fatigue performance of 18Ni300 maraging steel manufactured by laser powder bed fusion

Chola Elangeswaran^{1,*}, Kopila Gurung¹, Raphael Koch², Antonio Cutolo¹, Brecht Van Hooreweder¹

¹KU Leuven, Department of Mechanical Engineering, Celestijnenlaan 300, 3001 Leuven, Belgium

²Ford Research & Innovation Center Aachen, Süsterfeldstraße 200, 52072 Aachen, Germany

Abstract

This study investigates the fatigue behaviour of additively manufactured 18Ni300 maraging steel. Specifically, the surface and material parameters impacting fatigue performance are analysed through various post-treatment combinations. Vertically built miniaturised test samples produced by laser powder bed fusion are tested in as-built and age hardening heat treated conditions. To utilise the potential of using additive manufacturing for complex shaped parts in which conventional machining tools could have limited access, vibratory finishing and sand blasting are employed. The fatigue results show that in as-built microstructural condition, both the surface treatments significantly enhanced the fatigue performance, with vibratory finishing outperforming sand blasting owing to better surface finish. After heat treatment, sand blasted samples performed better than vibratory finished ones, due to higher residual stresses. This competing interaction between post-treatments sheds light on identifying the relative influence of various factors. With systematic post-fracture and microstructural analyses highlighting the fatigue influencing factors, recommendations are drawn to select post-treatments to achieve the desired fatigue performance.

Keywords: Additive manufacturing, Laser powder bed fusion, Maraging steel, Fatigue, SN curves

Nomenclature:

A: Material constant indicating y-intercept in Basquin's equation

AM: Additive manufacturing

AB: As-built state

b: Material constant indicating slope in Basquin's equation

d: Notch depth

HT: Heat treated state

* Correspondence: Chola Elangeswaran, KU Leuven, Department of Mechanical Engineering, Celestijnenlaan 300, 3001 Leuven, Belgium.

Email: chola.elangeswaran@kuleuven.be

URL: www.set.kuleuven.be/am

K_t : Elastic stress concentration factor

K_f : Fatigue notch factor

LPBF: Laser powder bed fusion

NT: Non-surface treated

q : Notch sensitivity index

S1, 1/2S2: XRD elastic constants

SB: Sand blasted

SLM: Selective laser melting

UTS: Ultimate tensile stress

VF: Vibratory finished

XRD: X-Ray Diffraction

1h820: Solutionized at 820° C for 1 hour

1h820+3h480: Solutionized at 820° C for 1 hour followed by age hardening at 480° C for 3 hours

N_f : Cycles to failure

3h480: Age hardening heat treated at 480° C for 3 hours

ΔK : Stress intensity factor range (MPa.m^{0.5})

σ_a : Stress amplitude (MPa)

σ_w : Endurance limit or fatigue limit (MPa)

ρ : Notch radius

1. Introduction

Additively manufactured high strength steels possess immense application potential in structural and functional components. The ability to build complex and intricate-shaped geometries through additive manufacturing (AM) enables to realise the designer's dreams for innovative product designs. AM has stepped into mainstream production environment for a handful of applications, including production of high added-value metal parts. Laser powder bed fusion (LPBF) or Selective Laser Melting (SLM) is a powder-bed metal AM process in which a part is built by selectively melting and fusing successive layers of powder using a laser beam¹.

18Ni300 maraging steel is a low carbon, age-hardenable martensitic steel capable of achieving exceptionally high strengths. The term 'maraging' denotes the martensitic age hardening heat treatment that produces intermetallic precipitates and results in unique mechanical properties². This alloy has proven its utility for different cyclic loading applications in the aerospace, hydrospace,

tooling industries, and recently in the automotive sector^{3,4}. Due to a growing interest for weight reduction in the automotive industry, topology optimised and complex-shaped designs are increasingly required to achieve effective strength-to-weight ratios. Therefore, applicability of additively manufactured maraging steel for such components has to be validated with appropriate post-treatments to achieve the desired fatigue performance.

LPBF-processed maraging steel exhibits a fine sub-grained cellular microstructure owing to the high cooling rates in the process⁵. This unique microstructure contributes to relatively high strengths and hardness compared to conventionally manufactured material in non-heat treated condition. The characteristic high tensile strengths in maraging steel are achieved after age hardening heat treatment resulting in the formation of intermetallic precipitates. Jägle et al.⁶ observed fine nanometre-sized precipitates, predominantly Ni-Ti rich ones, to be dispersed throughout the matrix. By varying the age hardening temperatures and times, Casati et al.⁵ found that different heat treatments led to varying proportions of reverted austenite, but this factor did not significantly influence the tensile behaviour. Precipitation hardening is known to be the primary strengthening mechanism of maraging steel. Such processability of maraging steel by LPBF and the resulting microstructure and tensile properties have been widely investigated^{7–11}, however, limited information is reported on the fatigue behaviour. Figure 1 shows an overview of high cycle fatigue results for vertically built, axial fully reversed loaded samples available in literature,^{12–15} containing data points extracted with reasonable degree of accuracy. The heat treated samples in Figure 1 are aged at varying temperatures and times within the commonly used age hardening regime.

The plot in Figure 1 shows an enhancement in fatigue behaviour for heat treated samples compared to as-built ones, albeit with some overlap. Differing part quality and microstructure-related factors can lead to inconsistencies in fatigue results among different research groups. The noteworthy fact is that all fatigue results shown in Figure 1, tests in other stress ratio^{16,17} ($R = 0$), rotary-bending mode^{18,19} and strain-controlled mode²⁰ were performed only on polished samples with very fine surface finish. Fatigue behaviour of a high strength material such as maraging steel is known to be highly sensitive to surface roughness. Moreover, since additive manufacturing is used to produce complex-shaped parts with internal geometries not easily accessible to machining tools, there is a need to investigate the fatigue behaviour on non-polished surfaces.

For reference, data points of vacuum melted and aged samples are plotted in Figure 1. LPBF-processed samples show reduced fatigue behaviour than the conventionally manufactured ones. Despite obtaining reliable tensile properties, this reduced fatigue performance is attributed to

process-induced pores and defects. Meneghetti et al.¹² observed 68% reduction in fatigue strength than the reference condition, mainly due to surface defects. Strain-based fatigue tests on polished samples done by Branco et al.²⁰ showed predominantly brittle fracture due to unmolten regions in the samples. Therefore, there is a requirement to optimise the process and evaluate post-treatments to achieve fatigue performance comparable to that of wrought maraging steel.

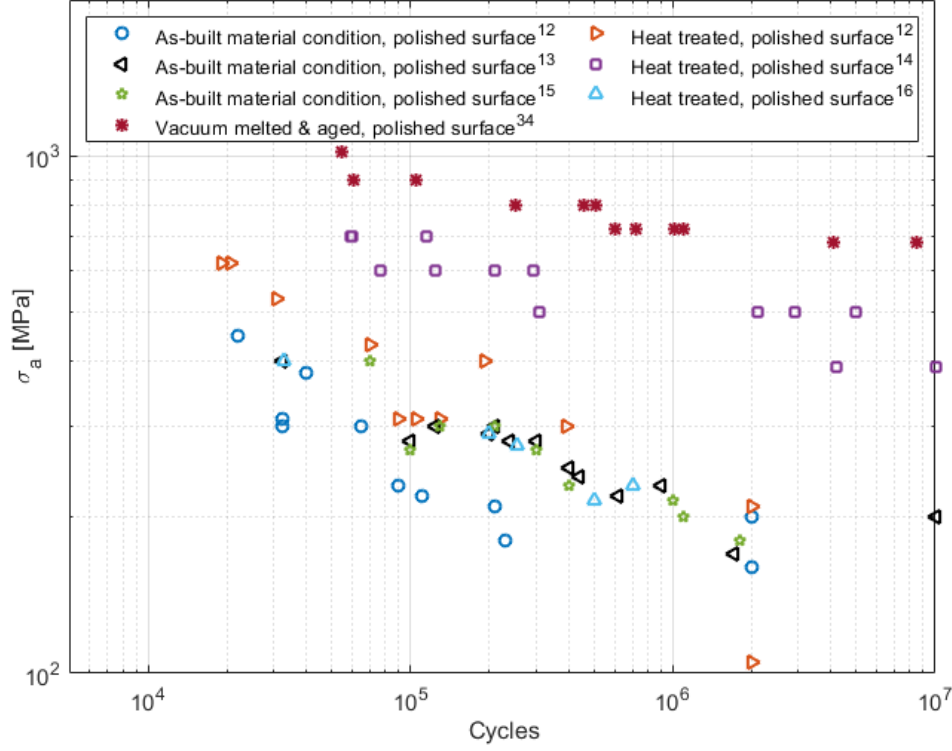


FIGURE 1 SN plot of vertically built maraging steel at different post-treatment conditions (data points are extracted from references)

The aforementioned shortcomings from state of the art are therefore addressed in this work by investigating the fatigue behaviour in three different surface conditions: non-surface treated, vibratory finished and sand blasted. All samples are tested in as-built and age hardening heat treated microstructural states. As expected, non-surface treated samples show very low fatigue performance of all the conditions. To improve the surface, vibratory finishing or mass finishing, an operation capable of treating internal surfaces of AM parts, is employed. Vibratory finished samples show considerably enhanced fatigue response, but still stopped short of reaching that of conventionally manufactured ones observed by Van Swam et al.²¹ Therefore, sand blasting, known to introduce beneficial compressive stresses, is employed as the third surface treatment. Sand blasted samples exhibit superior fatigue behaviour approaching that of conventionally manufactured condition. Post-fracture analyses are performed and empirical corrections are drawn to highlight the impact of fatigue influencing factors and select application-dependent post-treatments.

2. Materials and methods

Gas atomised 18Ni300 maraging steel (Material 1.2709) powder obtained from EOS GmbH was used for this research. Table 1 shows the chemical composition of the powder as provided by the supplier. The powder size distribution measured by Malvern Panalytical with their Morphologi range of equipment yielded the following results: D10 of 17.83 μm , D50 of 39.19 μm , and D90 of 58.55 μm . True density of powder measured by Quantochrome MVP-6DC multipycnometer was found to be 8.08 g/cm^3 . This true density was considered as the target theoretical density for subsequent LPBF parameter optimisation experiments. A ProX DMP 320 machine from 3D Systems, Inc. was used to build the samples. LPBF parameters were optimised for highest achievable relative density measured by Archimedes method. Varying laser powers from 100 W to 350 W with different levels of scan velocity, hatch distance and layer thickness yielded different sets of optimum parameters capable of manufacturing above 99.5% dense parts. Bidirectional scanning strategy was employed and the scan direction was rotated by 90° for each layer. Based on desirable melt pool shapes with adequate overlap, one optimum parameter set shown in Table 2 was chosen to build the samples for all heat treatments, tensile and fatigue tests. After chemically etching with 10% nital solution, light optical and scanning electron microscopy were performed with Keyence VHS 6000 and Philips XL30 FEG, respectively, to investigate the microstructures.

TABLE 1 Chemical composition of 18Ni300 maraging steel powder²²

Element	Fe	Co	Ni	Mo	Ti	Al	Cu	Cr	Mn	Si	C	P	S
Composition (wt. %)	Balance	8.69	18.04	4.74	0.75	0.10	0.03	0.21	0.06	0.08	0.01	<0.01	<0.01

TABLE 2 Optimum process parameter set

Laser power (W)	Scan velocity (mm/s)	Hatch distance (μm)	Layer thickness (μm)
200	1000	80	30

Heat treatments were performed in a vertical tube furnace in argon atmosphere at 10°C/min heating rate. Based on the maraging steel's phase diagram^{23,24} and recommended heat treatment procedures reported in literature^{25,26}, age hardening heat treatment was performed at 480° C for 3 hours. Some samples underwent a solutionizing treatment at 820° C for 1 hour, with and without being followed by the designated age hardening step. The notation of samples in different heat treated states are as follows: 'AB' for as-built state, '3h480' for age hardening heat treatment at 480° C for 3 hours, '1h820' for solutionizing at 820° C for 1 hour, and '1h820+3h480' for solutionizing at 820° C for 1

hour followed by age hardening at 480° C for 3 hours. The chosen heat treatment for fatigue testing is 1h820+3h480 as will be seen in section 3. Two different surface treatments were conducted on the fatigue samples, namely, vibratory finishing and sand blasting. In vibratory finishing the samples are agitated within a rotary vibratory chamber filled with wet abrasive medium. Also known as mass finishing, the process was performed by Rösler Oberflächentechnik GmbH. Cylindrical plastic chips of approximately 5 mm diameter and 10 mm length (proprietary name: RAM 4Z 1/2) were employed in a wet compound medium (proprietary name: RAM-C 21) under continuous water supply. To achieve the same surface finish, as-built and heat treated samples were processed for 7 hours and 14 hours, respectively, owing to higher hardness after heat treatment. Sand blasting was carried out in-house with a Straaltechniek International machine. Sharp-edged jagged red-brown corundum particles of grit size 0.8-1.2 mm were employed. The process was performed at 5 bar air pressure. Both the surface treatments were performed on fatigue samples directly built to final geometry. Residual stresses were measured using X-ray diffraction (XRD) technique with Seifert MZ IV goniometer equipped with Cr tube (40 kV, 30mA, 2.29 Å wavelength). The measurements were performed at (211) diffraction plane with $2\theta = 156^\circ$. The total scan range was set from 150° to 162° , at 1 second exposure time per step and 0.04° step size. The tilting angle (ψ) of X-ray tube was set from -45° to $+45^\circ$ and residual stresses were determined by $\sin^2\psi$ method explained by Vrancken²⁷. Since the diffraction peak is related with the strain, for varying values of ψ , the slope of strain vs $\sin^2\psi$ relationship indicates the sign of residual stress; a positive slope typically signifies tensile residual stress and vice versa. The X-ray elastic constants S1 and 1/2S2 for converting strains to stresses were $-1.271\text{E-}6$ and $5.811\text{E-}6$, respectively. Surface roughness along the gauge section was measured with a Mitutoyo Formtracer CS-3200S4 instrument. Three measurements were performed on each sample with an approximate 120° rotation. Vickers microhardness was measured on ground and polished cubes under 0.5 kg load with FV-700 instrument from Future-Tech Corporation. An average of at least five measurements were performed on the top surface (horizontal plane) of each sample. Quasi-static tensile tests were performed with an Instron 3367 machine at a strain rate of 0.5 mm/min according to ASTM E8 specifications. The sample geometry of the tensile test specimens is shown in Figure 2(a). These samples were vertically built along the longitudinal axis and tested in non-surface treated condition.

Axial tension-compression fatigue tests at $R = -1$ were performed with an Instron E10000 machine. The tests were performed on miniaturised circular cross sectional samples as shown in Figure 2(b), that were built vertically along the longitudinal direction. This miniaturised geometry was designed exclusively for additive manufacturing to minimise staircase effect on the surface, to reduce data

scatter by ascertaining fracture at the smallest section, and to avoid buckling while applying axial compressive loads. At the same time, the small sample geometry reduced the cost and time of manufacturing. This geometry was used in other published and internal studies and no significant deviations were found in the fatigue behaviour compared to standard-sized samples.^{28–31} Highly stressed volume approach as mentioned by Van Hooreweder et al.³² was utilised in designing the sample geometry. This design ensures that maximum stress is concentrated at the gauge section while maintaining fatigue notch factor K_f of unity. Tests were carried out at 30 Hz until total fracture or run-out at 2×10^6 cycles. Table 3 shows the different post-treatment combinations of the fatigue test campaign.

TABLE 3 Sample notations of different post-treatment conditions for fatigue testing

Notation	Material condition	Surface condition
AB NT	As-built	Non-surface treated
AB SB	As-built	Sand blasted
AB VF	As-built	Vibratory finished
HT NT	Heat treated	Non-surface treated
HT SB	Heat treated	Sand blasted
HT VF	Heat treated	Vibratory finished

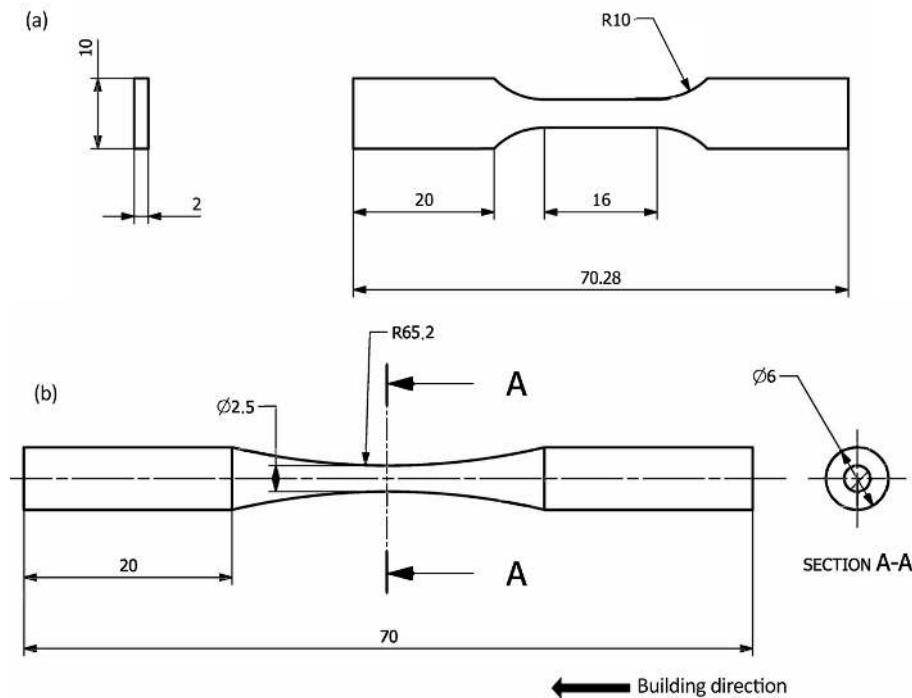


FIGURE 2 Tensile (a) and fatigue (b) sample geometry (all dimensions in mm)

3. Results

The samples manufactured with optimised process parameters exhibited a relative density of 99.73 ± 0.08 %. Table 4 shows the hardness in Vickers scale and tensile results. As-built condition exhibits a reasonable balance between strength and elongation to fracture. This mechanical behaviour is attributed to the unique microstructure obtained after LPBF, as will be seen in microstructural investigation. The low temperature heat treatment ‘3h480’ within the age hardening regime enhanced both the hardness and strength, clearly from the expected precipitation strengthening mechanism. Significant elongation before fracture is attained from the high temperature solutionizing treatment (1h820), at the expense of strength. Finally the solutionizing treatment followed by age hardening ‘1h820+3h480’ demonstrates the highest strengths with adequate elongation before fracture. Hence, this treatment is selected as the desired heat treatment for fatigue testing.

TABLE 4 Hardness and tensile results

Condition	Hardness (HV 0.5)	$\sigma_{y,0.2\%}$ (MPa)	UTS (MPa)	Elongation before fracture (%)
AB	393 \pm 14	1057 \pm 18	1176 \pm 13	13 \pm 0.4
3h480	605 \pm 8	1641 \pm 31	1726 \pm 29	5 \pm 1
1h820	323 \pm 24	834 \pm 9	938 \pm 11	15 \pm 1
1h820+3h480	615 \pm 19	1744 \pm 17	1786 \pm 7	5 \pm 1

Microstructures of the fatigue tested conditions, namely, as-built (AB) and heat treated (1h820+3h480) are shown in Figure 3. As-built maraging steel exhibits a melt pool-based morphological microstructure as seen in Figure 3(a). Figure 3(b) depicts a sub-grained cellular microstructure with cell sizes less than 1 μm . The moving heat source in the LPBF process forms molten pools and very high cooling rates with rapid solidification lead to such melt pool morphologies and cellular solidification within the pools. Aggregation of solute elements at cell boundaries, namely Ni, Mo and Ti enrichments, were etched away by the Nital reagent³³. Tan et al.³⁴ observed these cell boundaries to be populated with high density of dislocation networks. This elemental segregation and dislocation distribution along fine sub-grained cell walls are known to contribute towards the observed tensile behaviour.

After the age hardening heat treatment, the melt pool boundaries are dissolved and a lath martensitic microstructure is observed as shown in Figures 3(c) and (d). Precipitation hardening during heat treatment is known to produce finely dispersed nanometre-sized Ni_3M precipitates, predominantly

Ni₃Ti, which is the main strengthening phase²⁶. With high resolution TEM, Tan et al.³⁴ observed needle-shaped nanosized precipitates distributed throughout the matrix. Besides Ni₃M, coarser Fe₂Mo precipitation occurs along with dissolution of primary precipitates to form semi-coherent larger sized Laves phase^{26,35}. Bright spots resembling these Laves precipitates are observed at high magnification in Figure 3(d).

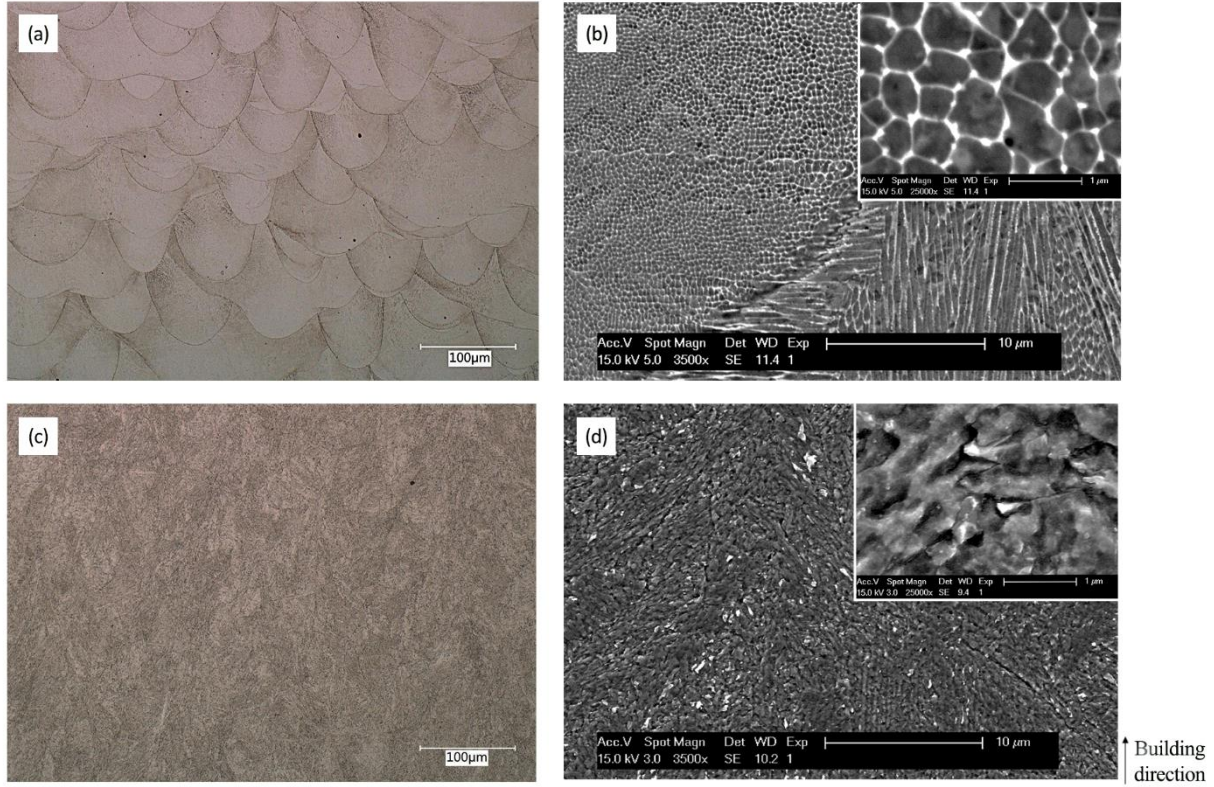


FIGURE 3 Microstructure of as-built condition in OM (a) and SEM (b), heat treated condition in OM (c) and SEM (d)

Surface roughness parameter Ra and residual stress values of all process conditions from Table 3 are shown in Table 5. No significant difference in roughness is observed between as-built and heat treated material conditions. The applied surface treatments clearly depict enhancement in surface finish. Compressive surface residual stresses were also introduced by both the surface treatments, with the heat treated samples showing higher stress magnitude for the same surface treatment. Figure 4 shows the fatigue results of all process conditions indicated in Table 3. SN curves are plotted on a log-log scale between stress amplitude (σ_a) and cycles to failure (N_f) as per Basquin's law shown in equation 1, with A and b as material constants. In as-built condition, non-surface treated (AB NT) samples exhibit the lowest fatigue behaviour, followed by sand blasted (AB SB) and vibratory finished (AB VF) ones in increasing order. After heat treatment, non-surface treated (HT NT) samples show a similar fatigue behaviour like AB NT, but with a steeper slope and reduced

performance at low stresses. The two surface treated samples show marked increase in fatigue performance. A different trend is observed after heat treatment, i.e. sand blasted samples perform better than vibratory finished ones. Reference test results for conventionally manufactured (vacuum melted and aged) and polished maraging steel reported by Van Swam et al.²¹ are also plotted in Figure 4. HT VF sample state is considered as comparable to the reference condition, due to similar age hardened microstructure and fine surface finish. It is seen that the fatigue performance of HT VF samples is lower than the reference. However, after sand blasting, the fatigue response of HT SB specimens approach that of conventionally manufactured samples.

$$\sigma_a = A. (2N_f)^b \quad (1)$$

TABLE 5 Surface roughness and surface residual stresses of fatigue tested conditions

Parameter	AB NT	AB VF	AB SB	HT NT	HT VF	HT SB
Roughness Ra (μm)	7.95 \pm 0.90	0.29 \pm 0.02	2.84 \pm 0.10	8.21 \pm 0.60	0.28 \pm 0.02	2.73 \pm 0.73
Residual stress (MPa)	+106 \pm 30	-383 \pm 27	-555 \pm 76	+63 \pm 24	-481 \pm 46	-696 \pm 52

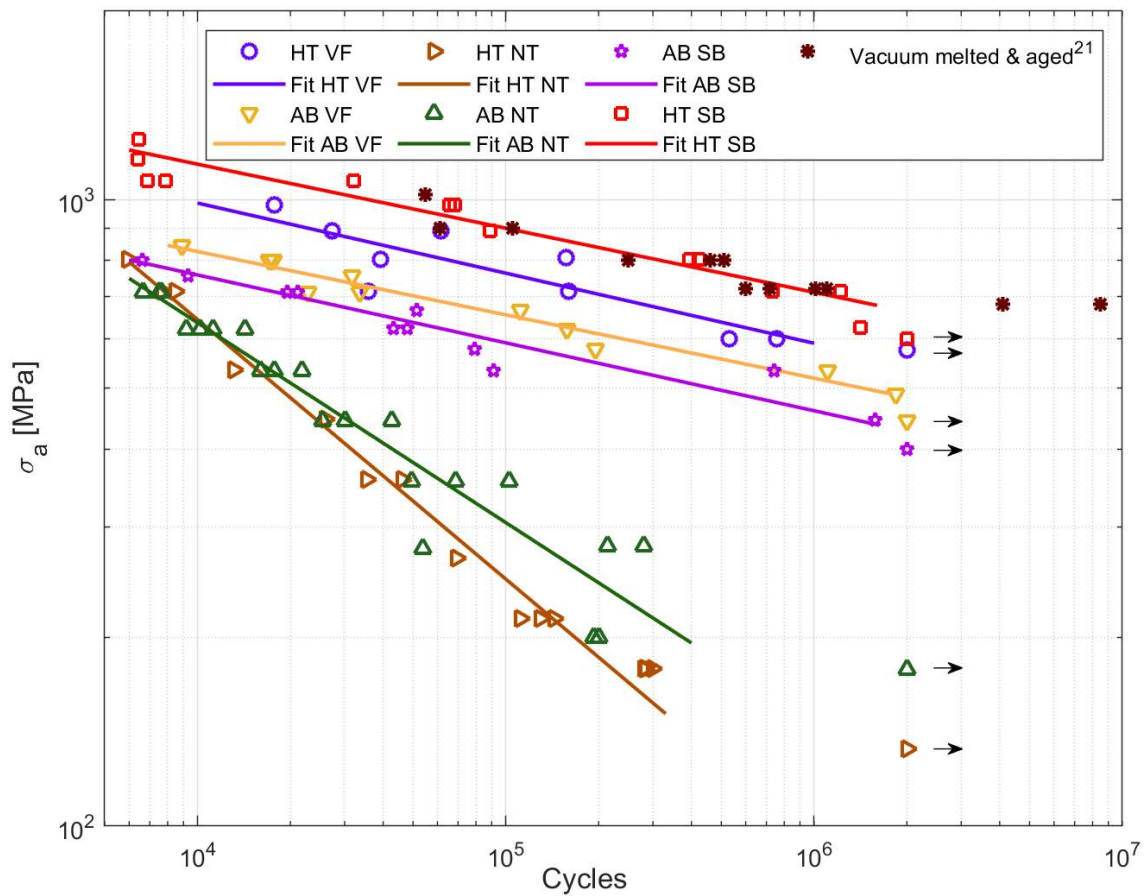


FIGURE 4 Fatigue SN plot of maraging steel (R = -1)

Figure 5 shows the fracture surfaces of the different sample conditions, all tested at 711 MPa stress amplitude. Cracks initiated from the surface and propagated toward the core for all the observed samples. The fracture surface consists of two main zones: crack initiation and propagation zone characterised by stepped ridges along crack growing direction, and final fracture zone characterised by dimples. The proportion of this initiation and propagation zone to final fracture zone depended on the stress level. Samples tested at higher stresses exhibited smaller initiation and propagation zone, and vice versa. For the non-surface treated conditions (AB NT and HT NT in Figures 5(a) and (g)), multiple crack initiation points are observed along the circumference. Especially HT NT sample shows a rough fracture surface with fracture planes oriented along different directions. The number of crack initiation points is related to surface roughness. A rough surface exhibits multiple stress concentration points favourable for crack initiation compared to a finer surface. Therefore, the rough surface in non-treated condition exhibits multiple crack initiation sites. Closer inspection in Figures 5(d) and (j) show that cracks initiated from surface defects. After vibratory finishing, the fracture surfaces in Figures 5(b) and (h) represent a typical fatigue fracture behaviour with a single crack initiating and propagating to cause the final rupture. As mentioned above, not many stress concentration points are available in a fine surface and therefore the first susceptible site led to crack initiation and growth. A sub-surface defect in Figure 5(e) is seen to have aided crack initiation in AB VF sample. HT VF sample shows a typical crack initiation from a surface facet as seen in Figure 5(k). After sand blasting, the intermediate surface roughness compared to the other two conditions depict reduced number of crack initiation points in Figures 5(c) and (i) compared to non-treated state, but higher than vibratory finished condition. Micrographs of crack initiation sites in Figures 5(f) and (l) closely resemble the non-surface treated counterparts.

4. Discussion

The most important factors that influence fatigue behaviour of LPBF maraging steel parts are keyhole pores, lack of fusion voids, surface finish, microstructure and residual stresses^{36–38}. The relative influence of each of these factors depends on the respective process condition. In low strength steels, high cycle fatigue performance generally improves with increasing tensile strengths. But in high strength steels such as maraging steel, intense deformation localisation could accelerate fatigue damage accumulation and lead to reduced fatigue strengths²¹. As a result, maraging steel typically exhibits an endurance limit approximating to 30 % of UTS, while endurance limit up to 50 % of UTS are observed for low strength steels³⁹. In the presence of aforementioned influencing factors such as porosity, defects, roughness and residual stresses, fatigue performance could further

be negatively impacted for LPBF samples. The influence of these factors are now discussed for each post-treatment combination and the fatigue strength at 2×10^6 cycles is compared and quantified.

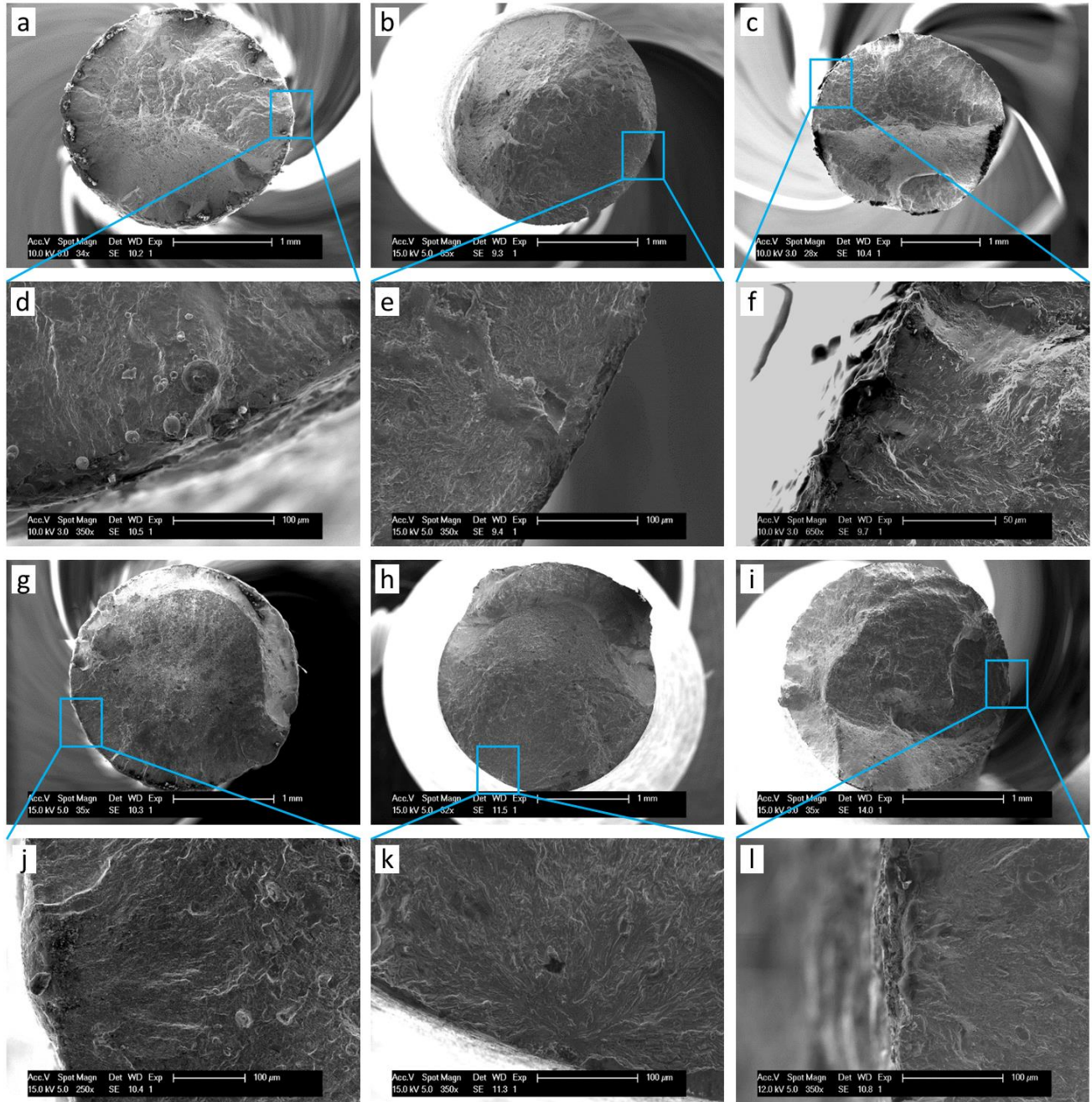


FIGURE 5 Fracture surfaces of all sample conditions tested at 711 MPa stress amplitude for: AB NT, 7527 cycles (a) and its crack initiation zone (d); AB VF, 23485 cycles (b) and its crack initiation zone (e); AB SB, 19525 cycles (c) and its crack initiation zone (f); HT NT, 8429 cycles (g) and its crack initiation zone (j); HT VF (h), 159439 cycles and its crack initiation zone (k); HT SB, 734330 cycles (i) and its crack initiation zone (l)

4.1 Fatigue behaviour of non-surface treated samples (AB NT and HT NT)

Non-surface treated samples exhibit the lowest fatigue performance. In as-built material condition, a low stress amplitude of 178 MPa corresponds to run-out at 2×10^6 cycles. Ratio of this run-out stress to tensile stress is found to be 0.15, far lower than the endurance limit to UTS ratio of 30% reported for conventionally manufactured, aged and polished samples. Microscopic observation of the multiple crack initiation points along the surface failed to indicate keyhole pores or lack of fusion voids as responsible factors for the failure. Therefore surface residual stresses and roughness could play influential roles on the resulting fatigue behaviour.

Very high cooling rates and temperature gradients in LPBF induce residual stresses which superimpose over the fatigue loads. But residual stress distribution is also dependent on sample geometry and building orientation, with long horizontal scan vectors inducing high stresses. Since the miniaturised samples in this research were built vertically, little influence of residual stresses is expected due to relatively short scan vectors in each layer. In as-built condition, XRD measurements on a surface perpendicular to the building direction showed a relatively low surface stress state of $+106 \pm 30$ MPa. Therefore, surface roughness seems more influential on the fatigue behaviour.

For the current vertically built samples, roughness is associated with two factors: layered surface topography from melt pool characteristics and unmolten powder particles sintered to the surface⁴⁰. Both these phenomena are visible in Figure 6(a) and (b), which show a fatigue sample's surface along the building direction. Spierings et al.⁴¹ theorised that the sintered powder particles do not lead to sharp stress concentration zones. The layered surface topography appears as a crest-trough system of wavy morphology, seemingly more influential towards inducing stress concentration. Figure 6(c) depicts fracture precisely along a trough. Microstructural observation showed deep and narrow melt pools after LPBF process. These melt pool depths spanning multiple layers along the building direction correspond to the distance between two troughs in Figure 6(a) and (b). Process parameter optimisation strategies offer room for improvement to tailor melt pool geometries and the resulting surface topography.

Figure 6(d) (left) shows the roughness profile of an AB NT sample along the gauge section. With a mean roughness of around $7.95 \mu\text{m Ra}$, high rising peaks and valleys are observed along the measured section. The valleys in such a surface act as sharp micro-notches and are most probable locations for crack nucleation, especially when coinciding with the troughs of surface topography. Optical microscopic surface profile of the sample that was cracked but not fully fractured is shown in

Figure 6(d) (right). From the colour scheming depicting trough to crest as blue to red, the crack is seen to exist precisely along the troughs (blue zones).

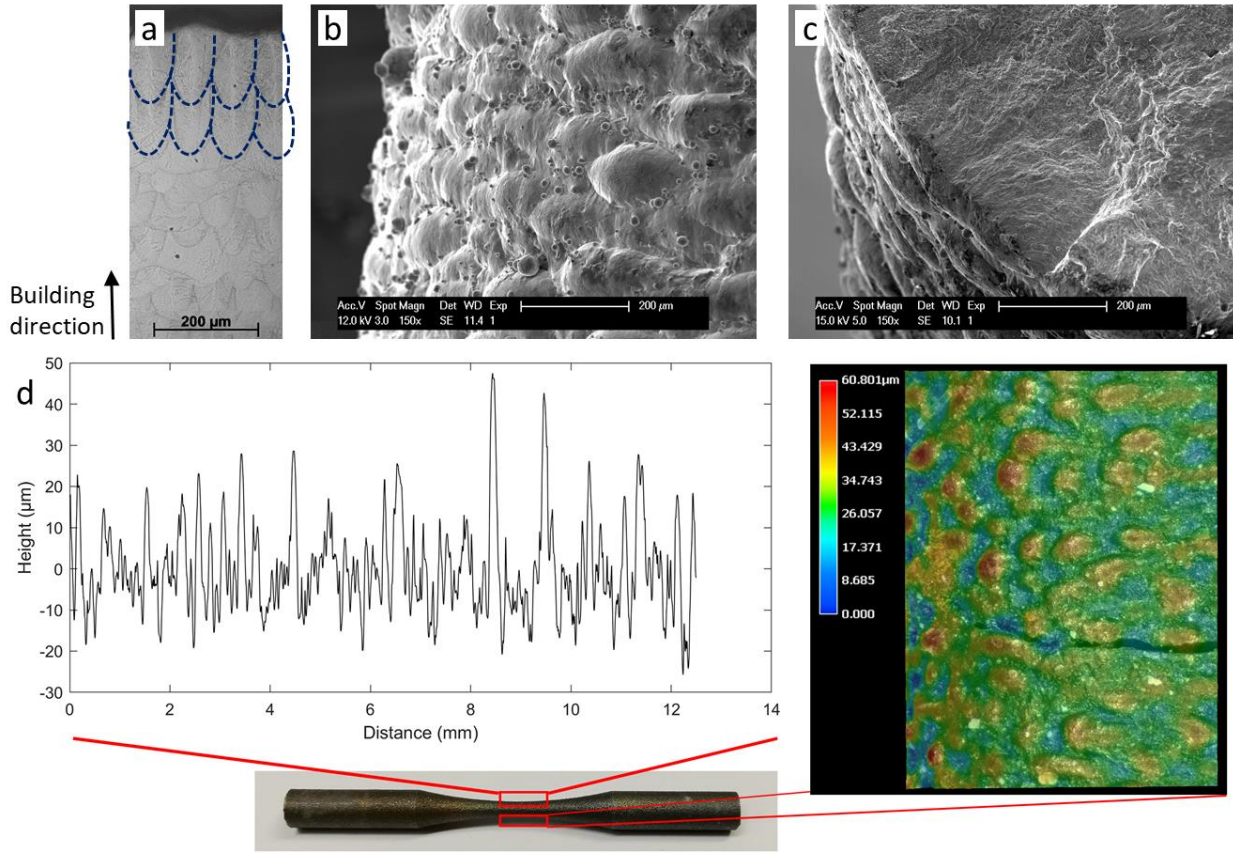


FIGURE 6 Melt pool morphology (a) leading to a wavy surface topography with crests and troughs (b), fracture occurring along the trough of the surface profile (c), roughness profile along the gauge section shows the height of peaks and valleys (left) and reconstructed cracked surface shows a crack growing along the troughs (right) (d)

The observations show that the rough surface in non-treated samples could essentially be considered to exhibit micro-notch effect. Such notched approximation for different surfaces were performed for wrought^{42–44} as well LPBF-processed metals,^{45,46} considering the surface valleys as elliptical notches. Similar elliptical notch approximation is considered for maraging steel in this work. The elastic stress concentration factor K_t for such a micro-notch based assumption is computed from equation 2⁴⁷.

$$K_t = 1 + 2 \sqrt{\frac{d}{\rho}} \quad (2)$$

where d is the notch depth and ρ is the notch radius. The notch depth is evaluated from surface roughness. Multiple roughness parameters have been used in literature to quantify notch effect.

Chan⁴⁸ and Kahlin⁴⁹ stated that maximum depth of the valley R_v is more representative to indicate the severity of micro-notches. Averaged parameter Ra and maximum profile height Rt were considered as depictive by Chan et al.⁵⁰ and Wycisk et al.,⁵¹ respectively. In this work, since multiple crack initiation points are seen across the circumference, one valley cannot be considered as representative for all stress concentration sites. Therefore, the averaged parameter Ra is used to quantify the notch effect. To account for multiple crack initiation points, notch radius is measured at ten deepest valleys for the representative surface roughness profile following the procedure reported by Pegues et al.⁴⁶ Using ImageJ software for the calculation resulted in average notch radius of 2.1 μm . Table 6 shows the computed notch effect parameters. In practice, K_t tends to be an overestimation and the actual peak stresses tend to be lower, due to small plastic zone near the notch tip and stress gradient perpendicular to the loading direction. Therefore, fatigue notch factor K_f is known to better approximate the influence of notch effect. K_f is given as ratio of endurance limit of unnotched sample ($\sigma_{e,unnotched}$) to that of notched sample ($\sigma_{e,notched}$), as shown in equation 3.

$$K_f = \frac{\sigma_{e,unnotched}}{\sigma_{e,notched}} \quad (3)$$

This fatigue notch factor is related with the stress concentration factor through fatigue notch sensitivity index of the material, q , as shown in equations 4 and 5. This index depends on the microstructure and notch radius and can vary from a value of 0 to 1; 0 meaning insensitive to notch and 1 indicating fully notch sensitive. For a given notch radius, high strength steels are more sensitive to notches than low strength steels.

$$K_f = 1 + q(K_t - 1) \quad (4)$$

$$q = \frac{K_f - 1}{K_t - 1} \quad (5)$$

Endurance limit was not measured in this work, so run-out stress at 2×10^6 cycles is considered for calculations. The parameters in Table 6 are computed considering AB VF condition as unnotched sample state, however, ignoring the residual stress state. In practice, surface treatment operations often induce residual stresses and the actual K_f and q could be much different. Computations from low stress polished surface are required to capture the actual influence of surface roughness. Therefore, with a known notch sensitivity from one roughness condition, the fatigue limit of other roughness values could be predicted for the same microstructural state from equation 3.

Table 6 Notch effect parameters of non-surface treated condition without considering surface residual stresses

Material condition	Stress concentration factor (K_t)	Fatigue notch factor (K_f)	Notch sensitivity index (q)
As-built	4.9	2.5	0.38
Heat treated	4.7	4.3	0.89

After age hardening heat treatment, the non-surface treated samples show similar performance like as-built ones, but with a steeper slope. High tensile strength obtained after age hardening is not reflected in the fatigue response. Considering run-out stress of HT VF as $\sigma_{e,unnotched}$, the calculated notch effect parameters are shown in Table 6. The results confirm the fact that a high notch sensitivity index is observed with high tensile strength after age hardening. As previously stated, these computations do not account for the influence of residual stresses. A dedicated notch effect study is required to validate these parameters in LPBF-processed maraging steel.

The slopes of both AB NT and HT NT samples in Figure 3 are found to be steeper than the other surface conditions. Rennert et al.⁵² and Stoffregen et al.⁵³ accounted for variations in surface roughness through slope of the SN curve, with rougher surfaces leading to steeper slopes. Therefore, due to higher roughness values, both non-surface treated conditions exhibit steep slopes, with HT NT's slope being even steeper due to higher notch sensitivity. These findings enable to conclude that for application parts in non-treated surface condition designed for high cycle fatigue regime, as-built material state could be preferred over heat treated state, however without utilising the beneficial effects of precipitation strengthening mechanism.

4.2 Fatigue behaviour of vibratory finished samples (AB VF and HT VF)

Significant fatigue performance enhancement is seen after vibratory finishing compared to non-surface treated state. Vibratory finishing resulted in a smooth surface removing the stress concentrators. Figures 7(a) and (b) show the surface along building direction free from waviness, unmolten powder particles and surface indentations. The number of crack initiation points also decreased to one, as seen in Figure 5(b) and (h). With a fine surface, not many sites for local stress concentrations are available; hence the first initiated crack propagated to cause the final fracture. This surface condition is closely comparable to mechanically ground surface. Therefore, gas pores, lack of fusion voids, residual stresses and microstructure influence the fatigue behaviour.

In as-built material condition, run-out stress of 445 MPa corresponds to 2×10^6 cycles. Ratio of this run-out stress to UTS is found to be 0.37, highlighting the possibility of attaining a higher fatigue limit to UTS ratio. This ratio is around 30% for conventionally manufactured and aged maraging

steel³⁹. The unique sub-grained cellular microstructure is understood to play an influential role on the observed fatigue response. With cell sizes less than 1 μm , the microstructure is composed of dense cellular network. From a fatigue crack initiation perspective, under applied cyclic loading, dislocations originating from the surface imperfections or microstructure inhomogeneities accumulate to attain sufficient strain energies to initiate a crack. In the presence of fine cellular microstructure, Liu et al.⁵⁴ theorised that this dislocation accumulation is slowed down by low angle cell wall networks acting as temporary barriers. This brief retardation could explain the extended fatigue lives. Detailed experimental validation with in-situ testing could facilitate in fully understanding this dislocation interaction and crack initiation mechanism in as-built maraging steel's microstructure.

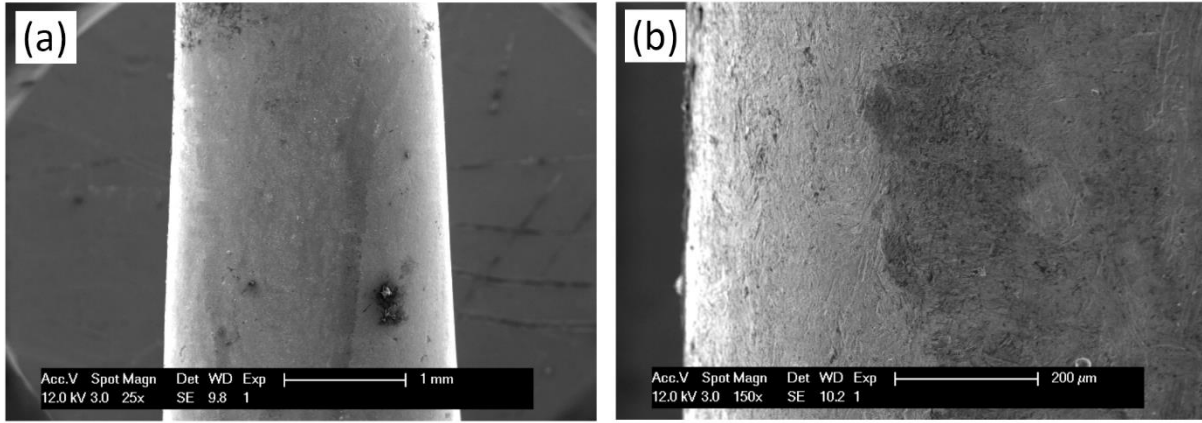


FIGURE 7 Surface of a vibratory finished sample in low (a) and high (b) magnification

From the microstructure and fracture surface investigations, very few influential pores or defects were found in the miniaturised samples. However, since formation of such flaws are sometimes inevitable in larger parts, their influence on the fatigue strength is now discussed. Fracture surface of a prematurely failed sample in Figure 5(e) shows a sub-surface defect influencing the crack initiation behaviour. Fracture mechanics approach captures the influence of flaws such as gas and keyhole pores, lack of fusion defects and inclusions, on the fatigue life. Murakami and Endo⁵⁵ proposed a geometrical parameter $\sqrt{\text{area}}$ to account for defects and cracks. $\sqrt{\text{area}}$ represents the square root of the defect when projected on a plane perpendicular to the loading direction. This method is widely employed for LPBF-processed metals.⁵⁶ Threshold stress intensity factor range and modified fatigue limit for a surface defect are given by equations 6 and 7, respectively⁵⁵.

$$\Delta K_{th,surface} = 3.33 \times 10^{-3} (HV + 120)(\sqrt{\text{area}})^{1/3} \quad (6)$$

$$\sigma_{w,surface} = \frac{1.43 (HV + 120)}{(\sqrt{area})^{1/6}} \quad (7)$$

where HV represents Vickers hardness and \sqrt{area} is calculated from the defect dimensions. The maximum size of the sporadically found flaws was measured to be around 25 to 30 μm . Figure 5(e) is a unique instance in which a non-spherical defect is observed and hence shown for illustration. Since sub-surface and internal defects also lead to fatigue crack initiations, corresponding fatigue limit formulations are shown in equations 8 and 9⁵⁷.

$$\sigma_{w,sub-surface} = \frac{1.40 (HV + 120)}{(\sqrt{area})^{1/6}} \quad (8)$$

$$\sigma_{w,internal} = \frac{1.56 (HV + 120)}{(\sqrt{area})^{1/6}} \quad (9)$$

Table 7 shows the values calculated for equations 6 to 8 for a defect size of 30 μm , without considering the influence of residual stresses. Crack growth experiments on LPBF maraging steel by Santos et al.⁵⁸ yielded a threshold stress intensity factor range of 5.2 $\text{MPa}\cdot\text{m}^{0.5}$, which is close to the defect-induced predicted parameter in Table 7. The calculated fatigue limit values for surface and sub-surface defects are lower than run-out stress, indicating that the samples are largely free of such defects and/or influenced by compressive residual stresses.

Compressive residual stress of -383 ± 27 MPa is observed at the surface. However, maximum stress amplitudes remain tensile during the entire testing regime. So crack initiation occurs at any defect-prone or stress concentration site. Microcrack propagation rate is however slowed under the influence of compressive residual stresses. Depth profile of the residual stress distribution was not performed in this study. The transition point from compressive to tensile stress state, if coincided with sub-surface defects, can be very detrimental for fatigue life. Such a residual stress distribution analysis could be beneficial in the future, especially while studying crack growth behaviour. The fatigue behaviour observed in vibratory finished samples is thus a combined effect of microstructure, defects and residual stress state. The influence of residual stress is more pronounced in sand blasted samples and further discussed in section 4.3.

TABLE 7 Theoretical fatigue limit calculations from defects

Material condition	Pore/defect size (μm)	$\Delta K_{th,surface}$ ($\text{MPa m}^{0.5}$)	$\sigma_{w,surface}$ (MPa)	$\sigma_{w,sub-surface}$ (MPa)	$\sigma_{w,internal}$ (MPa)	Run-out stress at 2×10^6 cycles
As-built	30	5.1	425	416	463	445
Heat treated	30	7.3	608	596	664	575

After heat treatment, vibratory finished (HT VF) samples exhibit an improved fatigue behaviour, exhibiting a run-out stress of 575 MPa at 2×10^6 cycles. Ratio of this run-out stress to UTS is found to be 0.32, indicating that fatigue limit to UTS ratio comparable to conventionally manufactured and aged maraging steel is achievable. Typically in aged maraging steels, Ti-based inclusions, lath martensitic boundaries and precipitate free zones are stated as favourable crack initiation sites.^{59,60} Dislocation slip originating from these zones under applied cyclic loading leads to strain localisation and crack initiation. So resisting dislocation motion would lead to enhanced crack initiation resistance. Reduced mobility of dislocations due to precipitates is the primary strengthening mechanism in maraging steels. Schnitzer et al.⁶¹ presented two possible means by which dislocations can overcome this resistance: (i) dislocations shearing through the precipitates, (ii) dislocations bowing around the precipitates known as Orowan mechanism. Various grades of maraging steel with differing ageing treatments demonstrate both types of strengthening mechanisms. For grade 300 maraging steel under the current heat treatment conditions, Orowan relationship is reported to account for the increase in strength^{2,21}. The size and dispersion of precipitates were not measured in this work, however, from similar studies on LPBF-processed maraging steel^{6,34}, Orowan mechanism is expected in HT VF samples as well. Therefore, this resistance for dislocation motion offered by the precipitates leads to delayed damage accumulation and crack initiation. However, once a crack is initiated, not much propagation resistance is observed as the precipitates are coherent with the matrix, leading to high crack growth rates³⁸.

The current HT VF condition, being closely relatable to conventionally manufactured and aged samples reported by Van Swam et al.²¹, exhibit a reduced fatigue performance than the latter. They also observed a higher UTS of 1916 MPa, compared to 1786 MPa in this work. This reduced tensile performance is likely to influence the reduction in fatigue behaviour, along with possible process-induced gas pores and defects. Formation of reverted austenite is commonly observed after the ageing heat treatment.^{9,33,62} Wang et al.⁶² state that the austenite phase being softer than martensite, can lead to reduced tensile strengths. However, they also mention that transformation-induced plasticity from austenite enhances the fatigue behaviour especially at high stresses. Therefore more investigation is required on quantifying the reverted austenite content and its influence on the mechanical behaviour.

Fracture surface images in Figures 5(h) and (k) depicted crack initiation from the surface. However, considering the sporadic flaw occurrence that could influence the fatigue strength, threshold stress intensity factor range and theoretical fatigue limits are calculated using equations 6 to 9. The values shown in Table 7 indicate higher calculated fatigue limits than the observed run-out stress.

Meneghetti et al.¹³ coupled El-Haddad parameter along with Murakami's $\sqrt{\text{area}}$ approach, to account for a smooth transition from short cracks (pores in this case) to long cracks in LPBF-processed maraging steel. Such a coupling results in reduced magnitude of predicted fatigue limits. Since porosity is not the prime concern of failures in this work, this approach is not investigated further. In cases where significant keyhole pores, lack of fusion defects and inclusions are observed, such detailed fracture mechanics approach is required to accurately model the fatigue behaviour. Besides, compressive surface residual stress is also expected to have influenced the fatigue behaviour, and follows similar discussion like AB VF condition. Residual stress impact is discussed in section 4.3 since the effect is more pronounced. As stated for AB VF condition, combined influence of microstructural aspects, defects and residual stresses result in the observed fatigue response of HT VF samples.

4.3 Fatigue behaviour of sand blasted samples (AB SB and HT SB)

Sand blasting resulted in enhanced fatigue performance compared to non-surface treated condition. In as-built state, 400 MPa stress level corresponds to run-out at 2×10^6 cycles, higher than that of non-treated but lower than vibratory finished samples. The sand blasted surfaces along building direction are shown in Figures 8(a) and (b). The wavy topography and sintered powder particles seen in non-treated surface are eliminated after sand blasting. Observed roughness of $2.84 \pm 0.10 \mu\text{m Ra}$ is lower than non-treated but higher than vibratory finished samples. During sand blasting, striking of high velocity particles on the material leads to indentations with small plastic deformation on the surface. Figure 8(b) shows the marks of indentation. The result is a compressive residual stress of -555 ± 76 MPa along the building direction.

The fatigue behaviour of a sand blasted surface is influenced by both surface roughness and residual stresses. The relative weightage of each factor's influence is however not straightforward. Using the procedure discussed in section 4.1, micro-notch effect parameters are computed for sand blasted surface. The resulting stress concentration factor K_t , fatigue notch factor K_f and notch sensitivity q are 3.3, 1.1 and 0.05, respectively. Run-out stress of AB VF condition was used to calculate K_f , without considering any residual stress corrections. The computed notch sensitivity is much lower than that of non-surface treated condition, clearly indicating that roughness is not the most severe influential factor. Therefore residual stresses have to be considered to explain the fatigue behaviour.

Residual stress superimposes over the mean stress. The resulting maximum stress is a combination of applied mean stress, applied stress amplitude and the induced residual stress. It is understood that during peak stress levels, certain surface spots of high stress concentration from micro-notch effect

act as preferential sites for crack initiation. This fact is evidenced by the multiple crack initiation points seen on fracture surface in Figure 5(c). Once a microcrack is initiated, tensile residual stress aids in crack opening. Compressive residual stress on the other hand impedes crack opening and lowers the growth rate. The stress distribution profile from the surface was not measured in this work; however, the transition from compressive to tensile stress zone influences the cracking behaviour. Lower microcrack propagation rates are encountered within the compressive stress region. Once the crack has grown over the transition towards tensile residual stress zone, high propagation rates are expected leading to fast fracture. Fatigue life of sand blasted samples can therefore be accounted for by the combined influence of micro-notch effects from the surface and compressive residual stresses. Correspondingly sand blasted samples' fatigue behaviour is observed higher than AB NT but lower than AB VF ones. Further investigation is required on the stress distribution profile and relating with crack growth characteristics.

Since residual stress is a constant stress in the sample, it is considered as a mean stress, however with some similarities and differences in this consideration. Residual stress is not uniformly distributed across the cross section. But the fact that crack initiation is mostly a surface phenomenon leads to this fair assumption of comparing with mean stress. With validated mean stress correction factors from approaches like Goodman, Gerber, Soderberg etc. for different load ratios, especially in the compressive mean stress regime, the influence of residual stress towards fatigue limit could be quantified. Different mean stress approaches are used in different research works for conventionally manufactured maraging steel. Such an extensive mean stress effect study is yet to be performed on LPBF-processed maraging steel.

After age hardening heat treatment, sand blasted samples (HT SB) exhibit the highest fatigue performance of all the conditions. The observed run-out stress of 600 MPa at 2×10^6 cycles is higher than that of vibratory finished samples, despite possessing a rougher surface. Very high compressive stresses of up to -696 ± 52 MPa seems to have significantly influenced the crack initiation and propagation behaviour.

Residual stresses induced on a surface during sand blasting or shot peening depends on the hardness of the material. Generally for shot peening on a softer material, the plastically deformed portion is predominantly responsible for the induced compressive stresses. The extent of deformation of surface layers determines the surface residual stress magnitude. On a harder material, the plastic deformation is lower and the magnitude of stress induced in the sub-surface material is higher and vice versa, for the same peening conditions⁶³. Since the hardness of maraging steel is significantly

increased after age hardening heat treatment, higher compressive stress magnitude is observed after sand blasting. If HT VF condition is considered as unnotched sample condition to compute micro-notch effect, fatigue notch factor K_f is found to be 0.95. K_f less than 1, with run-out stress of HT SB higher than HT VF, indicates that surface roughness is not a significantly influential parameter. This finding confirms the fact that fatigue performance of high strength steels can be improved by compressive stresses even with surface imperfections.

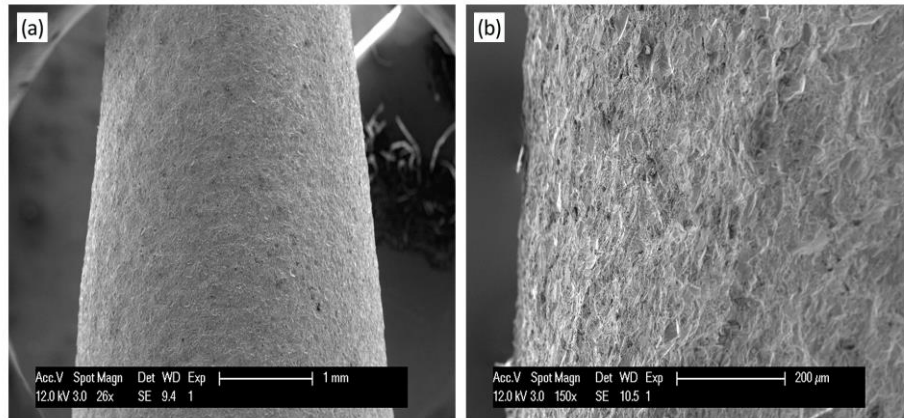


FIGURE 8 Surface of a sand blasted sample in low (a) and high (b) magnification

The SN curve of HT SB condition approaches the data points of conventionally manufactured maraging steel reported by Van Swam et al.²¹ Approximately 34% run-out stress to UTS ratio indicates that such compressive stress inducing operations can be preferred when high fatigue strengths are required. In view of the combined roughness and compressive stress influence, the latter seems to clearly dominate over the micro-notch effect of the former. However, since multiple crack initiation points are still observed along the surface, a finer surface with compressive stress state could be expected to result in much higher fatigue strengths; more investigation is necessary to verify this aspect.

4.4 Competing interaction and selection of post-treatments

As discussed in sections 4.2 and 4.3, the two surface treatments competitively interact between the two material conditions. In as-built condition, vibratory finished samples perform better than sand blasted ones. After heat treatment, the reverse is observed; sand blasted samples show superior fatigue behaviour. The reason for this anomaly lies in the interaction between microstructure, hardness and surface condition. In as-built state, sand blasting introduced beneficial compressive stresses in the sample, but seemingly not high enough to override the detrimental effects of higher

surface roughness. After vibratory finishing, the surface was free of stress concentrators leading to delayed crack initiation.

After heat treatment, precipitation hardening resulted in high hardness, which in turn led to very high magnitude of compressive stresses after sand blasting. This beneficial stress state seems to have diminished the surface roughness effect. Superposition of residual stress with the applied tension-compression stress leads to high proportion of sample test loads to be in compression regime, which is beneficial for fatigue life.

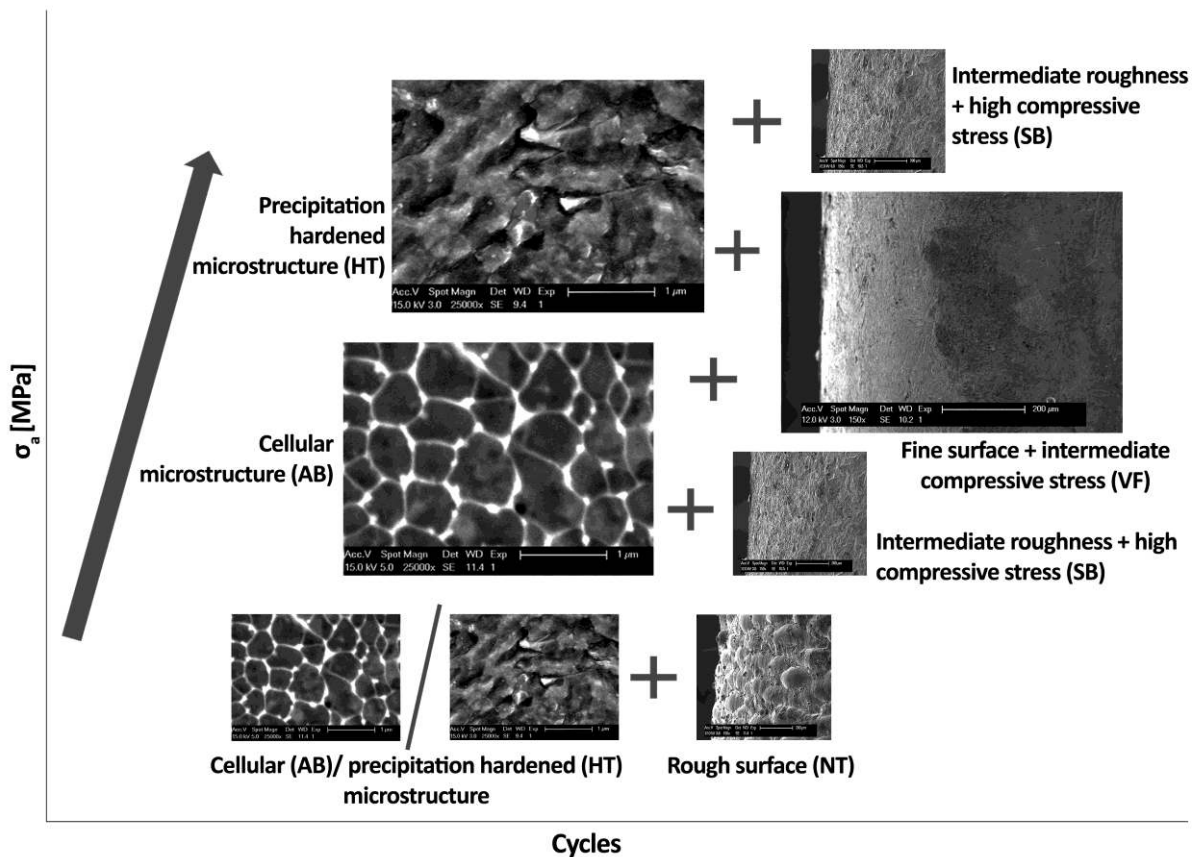


FIGURE 9 Combination of microstructural and surface conditions for increasing fatigue performance

Summary of the microstructure and surface condition combinations for increasing fatigue lives is shown in Figure 9. For distinction, non-treated surface (NT) is indicated as rough surface, sand blasted (SB) as intermediate roughness and vibratory finished (VF) as fine surface. Residual stresses are indicated as intermediate for vibratory finished and high for sand blasted sample conditions. The figure shows the trend of interactions and ability to predict fatigue performance of new post-treatments. In as-built (AB) cellular microstructure, very fine surface finishing operations such as grinding and polishing could be preferred. With precipitation hardened heat treated (HT)

microstructure, high compressive stress inducing operations like shot peening or laser shock peening could be expected to perform better. Suitable combination of heat treatment and surface treatment can therefore be selected based on the application part requirements. Conventional use cases of maraging steel include high strength applications, but as-built LPBF parts can be used when reasonable ductility is a requirement. When choosing for fatigue lives, non-treated surface is clearly not desirable. Age hardening heat treatment with a suitable surface treatment is recommended, considering that fine surface finish is generally preferred for both functional performance and aesthetic appeal. Vibratory finishing is a suitable operation for additive manufacturing as it can treat complex shaped parts and internal geometries. At localised members where high compressive stress is required, sand blasting can be performed to utilise its beneficial effects. As heat treated and sand blasted parts approach the fatigue behaviour of conventionally manufactured maraging steel, LPBF with the right combination of post-treatments holds immense potential for high strength applications.

5. Conclusion

Maraging steel manufactured by laser powder bed fusion, with the right choice of post-treatments, exhibits comparable fatigue behaviour to conventionally manufactured samples. Depending on the application loading and surface requirements, appropriate post-treatments can be selected.

- With no surface treatment, both as-built and heat treated samples exhibit similar fatigue behaviour. Influence of micro-notches from rough surface dominates the fatigue life leading to early failures.
- Fatigue performance is significantly enhanced by surface treatments, namely, vibratory finishing and sand blasting.
- In as-built microstructural condition, vibratory finished samples perform better than sand blasting, due to the fine surface finish obtained from the former.
- After heat treatment, sand blasting introduced higher magnitudes of beneficial compressive stresses in the samples, enhancing the fatigue life compared to vibratory finished specimens.

Acknowledgement

This research was conducted with the financial support of Ford Motor Company under Ford-KU Leuven University Research Alliance Framework KUL-0002 for the project ‘Durable Metal AM Components’. The authors would like to thank Arthur Smet for the insightful master’s thesis, Louis Depre for performing residual stress measurements and Rösler Oberflächentechnik GmbH for performing the vibratory finishing operation.

Conflict of interest: None

Bibliography

- 1 Kruth JP, Froyen L, Van Vaerenbergh J, Mercelis P, Rombouts M, Lauwers B. Selective laser melting of iron-based powder. *J Mater Process Technol.* 2004;149: 616–622.
- 2 Floreen S. The physical metallurgy of maraging steels. *Metall Rev.* 1968;13: 115–128.
- 3 Hall AM, Slunder CJ. The Metallurgy, Behavior, and Application of the 18-Percent Nickel Maraging Steels. *Natl Aeronaut Sp Adm.* 1968: 141.
- 4 NeoNickel. Maraging Steels in Automotive Shafts and Aircraft Landing Gears - NeoNickel. Available at: <https://www.neonickel.com/technical-resources/technical-papers/maraging-steels-automotive-shafts-aircraft-landing-gears/>. Accessed March 29, 2019.
- 5 Casati R, Lemke J, Tuissi A, Vedani M. Aging Behaviour and Mechanical Performance of 18-Ni 300 Steel Processed by Selective Laser Melting. *Metals (Basel).* 2016;6: 218.
- 6 Jäggle EA, Sheng Z, Wu L, et al. Precipitation Reactions in Age-Hardenable Alloys During Laser Additive Manufacturing. *Jom.* 2016;68: 943–949.
- 7 Demir AG, Previtali B. Investigation of remelting and preheating in SLM of 18Ni300 maraging steel as corrective and preventive measures for porosity reduction. *Int J Adv Manuf Technol.* 2017;93: 2697–2709.
- 8 Hermann Becker T, Dimitrov D. The achievable mechanical properties of SLM produced Maraging Steel 300 components. *Rapid Prototyp J.* 2016;22: 487–494.
- 9 Suryawanshi J, Prashanth KG, Ramamurty U. Tensile, fracture, and fatigue crack growth properties of a 3D printed maraging steel through selective laser melting. *J Alloys Compd.* 2017;725: 355–364.
- 10 Kempen K, Yasa E, Thijs L, Kruth JP, Van Humbeeck J. Microstructure and mechanical properties of selective laser melted 18Ni-300 steel. *Phys Procedia.* 2011;12: 255–263.
- 11 Yasa E, Deckers J, Kruth J-P, Rombouts M, Luyten J. Charpy impact testing of metallic selective laser melting parts. *Virtual Phys Prototyp.* 2010;5: 89–98.
- 12 Meneghetti G, Rigon D, Cozzi D, Waldhauser W, Dabalà M. Influence of build orientation on static and axial fatigue properties of maraging steel specimens produced by additive manufacturing. *Procedia Struct Integr.* 2017;7: 149–157.

- 13 Meneghetti G, Rigon D, Gennari C. An analysis of defects influence on axial fatigue strength of maraging steel specimens produced by additive manufacturing. *Int J Fatigue*. 2018;118: 54–64.
- 14 Damon J, Hanemann T, Dietrich S, Graf G, Lang KH, Schulze V. Orientation dependent fatigue performance and mechanisms of selective laser melted maraging steel X3NiCoMoTi18-9-5. *Int J Fatigue*. 2019;127: 395–402.
- 15 Rigon D, Meneghetti G, Görtler M, Cozzi D, Waldhauser W, Dabalà M. Influence of defects on axial fatigue strength of maraging steel specimens produced by additive manufacturing.
- 16 Branco R, Silva J, Ferreira JM, et al. Fatigue behaviour of maraging steel samples produced by SLM under constant and variable amplitude loading. *Procedia Struct Integr*. 2019;22: 10–16.
- 17 Santos LMS, Ferreira JAM, Jesus JS, Costa JM, Capela C. Fatigue behaviour of selective laser melting steel components. 2016.
- 18 Croccolo D, De Agostinis M, Fini S, et al. Sensitivity of direct metal laser sintering Maraging steel fatigue strength to build orientation and allowance for machining. *Fatigue Fract Eng Mater Struct*. 2019;42: 374–386.
- 19 Croccolo D, De Agostinis M, Fini S, et al. Fatigue Response of As-Built DMLS Maraging Steel and Effects of Aging, Machining, and Peening Treatments. *Metals (Basel)*. 2018;8: 505.
- 20 Branco R, Costa J, Berto F, et al. Low-Cycle Fatigue Behaviour of AISI 18Ni300 Maraging Steel Produced by Selective Laser Melting. *Metals (Basel)*. 2018;8: 32.
- 21 Van Swam LF, Pelloux RM, Grant NJ. Fatigue behavior of maraging steel 300. *Metall Trans A*. 1975;6: 45–54.
- 22 EOS GmbH. *Mill Test Certificate: EOS Maraging Steel MS1*. Krailing, Germany; 2017.
- 23 Takata N, Nishida R, Kato M, Suzuki A, Kobashi M. Crystallographic Features of Microstructure in Maraging Steel Fabricated by Selective Laser Melting. *Metals (Basel)*. 2018;8: 440.
- 24 Goldstein JI, Ogilvie RE. *Fe-Ni Phase Diagram*. Greenbelt. Maryland; 1965.
- 25 Yin S, Chen C, Yan X, et al. The influence of aging temperature and aging time on the mechanical and tribological properties of selective laser melted maraging 18Ni-300 steel.

Addit Manuf. 2018;22: 592–600.

- 26 Zhu F, Yin YF, Faulkner RG. Microstructural control of maraging steel C300. *Mater Sci Technol.* 2011;27: 395–405.
- 27 Vrancken B. Study of Residual Stresses in Selective Laser Melting. *PhD Thesis; KU Leuven Arenb Dr Sch Fac Eng Sci.* 2016.
- 28 Van Hooreweder B. Development of Accelerated Multi-axial Fatigue Tests Based on Scaling Laws (Ontwikkeling van versnelde multi-axiale levensduurtesten op basis van schaalwetten). 2013.
- 29 Elangeswaran C, Cutolo A, Muralidharan GK, et al. Effect of post-treatments on the fatigue behaviour of 316L stainless steel manufactured by laser powder bed fusion. *Int J Fatigue.* 2019;123: 31–39.
- 30 Cutolo A, Elangeswaran C, de Formanoir C, Muralidharan GK, Van Hooreweder B. Effect of Heat Treatments on Fatigue Properties of Ti–6Al–4V and 316L Produced by Laser Powder Bed Fusion in As-Built Surface Condition. In: Springer, Cham; 2019:395–405.
- 31 Beevers E. Fatigue of Ti6Al4V samples produced by Selective Laser Melting. 2016.
- 32 Hooreweder B Van, Boonen R, Moens D, Kruth J, Sas P. On the determination of fatigue properties of Ti6Al4V produced by selective laser melting. *Struct Dyn Mater Conf.* 2012: 1–9.
- 33 Bai Y, Yang Y, Wang D, Zhang M. Influence mechanism of parameters process and mechanical properties evolution mechanism of maraging steel 300 by selective laser melting. *Mater Sci Eng A.* 2017;703: 116–123.
- 34 Tan C, Zhou K, Kuang M, Ma W, Kuang T. Microstructural characterization and properties of selective laser melted maraging steel with different build directions. *Sci Technol Adv Mater.* 2018;19: 746–758.
- 35 Simm TH, Sun L, Galvin DR, et al. The effect of a two-stage heat-treatment on the microstructural and mechanical properties of a maraging steel. *Materials (Basel).* 2017;10: 1–24.
- 36 DebRoy T, Wei HL, Zuback JS, et al. Additive manufacturing of metallic components – Process, structure and properties. *Prog Mater Sci.* 2018;92: 112–224.
- 37 Schijve J. *Fatigue of Structures and Materials.* Second Edi. Springer Science & Business

Media; 2009.

- 38 Grosskrutz JC. Strengthening and Fracture in Fatigue. (Approaches for Achieving High Fatigue Strength). *Met Trans.* 1972;3: 1255–1262.
- 39 Karliński W, Tacikowski J, Wojtyra K. Fatigue strength of nitrided 18Ni250 and 18Ni300 grade maraging steels. *Surf Eng.* 1999;15: 483–489.
- 40 Thijs L, Verhaeghe F, Craeghs T, Humbeeck J Van, Kruth JP. A study of the microstructural evolution during selective laser melting of Ti-6Al-4V. *Acta Mater.* 2010;58: 3303–3312.
- 41 Spierings AB, Starr TL, Wegener K. Fatigue performance of additive manufactured metallic parts. *Rapid Prototyp J.* 2013;19: 88–94.
- 42 Taylor D, Clancy OM. THE FATIGUE PERFORMANCE OF MACHINED SURFACES. *Fatigue Fract Eng Mater Struct.* 1991;14: 329–336.
- 43 Arola D, Williams CL. Estimating the fatigue stress concentration factor of machined surfaces. *Int J Fatigue.* 2002;24: 923–930.
- 44 Guillemot N, Lartigue · C, Billardon · R, Mawussi · B K. Prediction of the endurance limit taking account of the microgeometry after finishing milling. *Int J Interact Des Manuf.* 2010;4: 239–249.
- 45 Hovig EW, Azar AS, Sunding MF, Andreassen E, Sørby K. High cycle fatigue life estimation of materials processed by laser powder bed fusion. *Fatigue Fract Eng Mater Struct.* 2019;42: 1454–1466.
- 46 Pegues JW, Shamsaei N, Roach MD, Williamson RS. Fatigue life estimation of additive manufactured parts in the as-built surface condition. *Mater Des Process Commun.* 2019;1: e36.
- 47 Pikelley W. *Peterson's Stress Concentration Factors*. Second Edi. New York: John Wiley & Sons, Inc.; 1997.
- 48 Chan KS. Characterization and analysis of surface notches on Ti-alloy plates fabricated by additive manufacturing techniques. *Surf Topogr Metrol Prop.* 2015;3: 044006.
- 49 Kahlin M, Ansell H, Moverare JJ. Fatigue behaviour of notched additive manufactured Ti6Al4V with as-built surfaces. *Int J Fatigue.* 2017;101: 51–60.
- 50 Chan KS, Koike M, Mason RL, Okabe T. Fatigue life of titanium alloys fabricated by additive

layer manufacturing techniques for dental implants. *Metall Mater Trans A Phys Metall Mater Sci*. 2013;44: 1010–1022.

- 51 Wycisk E, Solbach A, Siddique S, Herzog D, Walther F, Emmelmann C. Effects of defects in laser additive manufactured Ti-6Al-4V on fatigue properties. *Phys Procedia*. 2014;56: 371–378.
- 52 Rennert R, Kullig E, Vormwald M, Esderts A, Siegele D. *Analytical Strength Assessment of Components*. 6th ed. (FKM, ed.). Frankfurt am Main: VDMA Verlag; 2012.
- 53 Stoffregen HA, Butterweck K, Abele E. Fatigue Analysis in Selective Laser Melting: Review and Investigation of Thin-Walled Actuator Housings. *Solid Free Fabr Proc*. 2014: 635–650.
- 54 Liu L, Ding Q, Zhong Y, et al. Dislocation network in additive manufactured steel breaks strength–ductility trade-off. *Mater Today*. 2018;21: 354–361.
- 55 Murakami Y, Endo M. Effects of hardness and crack geometries on ΔK_{th} of small cracks emanating from small defects. In: Miller KJ, de los Rios ER, eds. *The Behaviour of Short Fatigue Cracks*. Vol EGF Pub. 1. London: Mechanical Engineering Publications; 1986:275–293.
- 56 Yadollahi A, Mahtabi MJ, Khalili A, Doude HR, Newman JC. Fatigue life prediction of additively manufactured material: Effects of surface roughness, defect size, and shape. *Fatigue Fract Eng Mater Struct*. 2018;41: 1602–1614.
- 57 MURAKAMI Y. Effects of Small Defects and Nonmetallic Inclusions on the Fatigue Strength of Metals. *JSME Int journal Ser I, Solid Mech strength Mater*. 1989;32: 167–180.
- 58 Santos LMS, Ferreira JAM, Jesus JS, Costa JM, Capela C. Fatigue behaviour of selective laser melting steel components. *Theor Appl Fract Mech*. 2016;85: 9–15.
- 59 Garrison WM, Banerjee MK. Martensitic Non-Stainless Steels: High Strength and High Alloy. In: *Reference Module in Materials Science and Materials Engineering*. Elsevier; 2018.
- 60 Xu ZK, Wang B, Zhang P, Zhang ZF. A fast evaluation method for fatigue strength of maraging steel: The minimum strength principle. *Mater Sci Eng A*. June 2020: 139659.
- 61 Schnitzer R, Zinner S, Leitner H. Modeling of the yield strength of a stainless maraging steel. *Scr Mater*. 2010;62: 286–289.
- 62 Wang B, Zhang P, Duan QQ, et al. Optimizing the fatigue strength of 18Ni maraging steel

through ageing treatment. *Mater Sci Eng A*. 2017;707: 674–688.

- 63 Wohlfahrt H. The Influence Of Peening Conditions On The Resulting Distribution Of Residual Stress. In: *International Conferences on Shot Peening ICSP-2*. Chicago; 1984:316–331.